# XENON1T dark matter data analysis: Signal reconstruction, calibration, and event selection

E. Aprile, <sup>1</sup> J. Aalbers, <sup>2,3</sup> F. Agostini, <sup>4</sup> M. Alfonsi, <sup>5</sup> L. Althueser, <sup>6</sup> F. D. Amaro, <sup>7</sup> V. C. Antochi, <sup>2</sup> F. Arneodo, <sup>8</sup> L. Baudis, <sup>9</sup> B. Bauermeister, <sup>2</sup> L. Bellagamba, <sup>4</sup> M. L. Benabderrahmane, <sup>8</sup> T. Berger, <sup>10</sup> P. A. Breur, <sup>3</sup> A. Brown, <sup>9</sup> E. Brown, <sup>10</sup> S. Bruenner, <sup>11</sup> G. Bruno, <sup>8</sup> R. Budnik, <sup>12</sup> C. Capelli, <sup>9</sup> J. M. R. Cardoso, <sup>7</sup> D. Cichon, <sup>11</sup> D. Coderre, <sup>13</sup> A. P. Colijn, <sup>3,\*</sup> J. Conrad, <sup>2</sup> J. P. Cussonneau, <sup>14</sup> M. P. Decowski, <sup>3</sup> P. de Perio, <sup>1</sup> P. Di Gangi, <sup>4</sup> A. Di Giovanni, <sup>8</sup> S. Diglio, <sup>14</sup> A. Elykov, <sup>13</sup> G. Eurin, <sup>11</sup> J. Fei, <sup>15</sup> A. D. Ferella, <sup>2</sup> A. Fieguth, <sup>6</sup> W. Fulgione, <sup>16,17</sup> A. Gallo Rosso, <sup>16</sup> M. Galloway, <sup>9</sup> F. Gao, <sup>1</sup> M. Garbini, <sup>4</sup> L. Grandi, <sup>18</sup> Z. Greene, <sup>1</sup> C. Hasterok, <sup>11,‡</sup> E. Hogenbirk, <sup>3</sup> J. Howlett, <sup>1</sup> M. Iacovacci, <sup>19</sup> R. Itay, <sup>12</sup> F. Joerg, <sup>11</sup> S. Kazama, <sup>20</sup> A. Kish, <sup>9</sup> G. Koltman, <sup>12</sup> A. Kopec, <sup>21</sup> H. Landsman, <sup>12</sup> R. F. Lang, <sup>21</sup> L. Levinson, <sup>12</sup> Q. Lin, <sup>1</sup> S. Lindemann, <sup>13</sup> M. Lindner, <sup>11</sup> F. Lombardi, <sup>7</sup> J. A. M. Lopes, <sup>7,†</sup> E. López Fune, <sup>22</sup> C. Macolino, <sup>23</sup> J. Mahlstedt, <sup>2</sup> A. Manfredini, <sup>9,12</sup> F. Marignetti, <sup>19</sup> T. Marrodán Undagoitia, <sup>11</sup> J. Masbou, <sup>14</sup> D. Masson, <sup>21</sup> S. Mastroianni, <sup>19</sup> M. Messina, <sup>16,8</sup> K. Micheneau, <sup>14</sup> K. Miller, <sup>18</sup> A. Nolinario, <sup>16</sup> K. Morå, <sup>2</sup> Y. Mosbacher, <sup>12</sup> M. Murra, <sup>6</sup> J. Naganoma, <sup>16,24</sup> K. Ni, <sup>15</sup> U. Oberlack, <sup>5</sup> K. Odgers, <sup>10</sup> B. Pelssers, <sup>8</sup> R. Peres, <sup>9,7</sup> F. Piastra, <sup>9</sup> J. Pienaar, <sup>18</sup> V. Pizzella, <sup>11</sup> G. Plante, <sup>1</sup> R. Podviianiuk, <sup>16</sup> H. Qiu, <sup>12</sup> D. Ramírez García, <sup>13</sup> S. Reichard, <sup>8</sup> B. Riedel, <sup>18</sup> A. Rizzo, <sup>1</sup> A. Rocchetti, <sup>13</sup> N. Rupp, <sup>11</sup> J. M. F. dos Santos, <sup>7</sup> G. Sartorelli, <sup>4</sup> N. Šarčević, <sup>13</sup> M. Scheibelhut, <sup>5</sup> S. Schindler, <sup>5</sup> J. Schreiner, <sup>11</sup> D. Schulte, <sup>6</sup> M. Schumann, <sup>13</sup> L. Scotto Lavina, <sup>22</sup> M. Selvi, <sup>4</sup> P. Shagin, <sup>24</sup> E. Shockley, <sup>18</sup> M. Silva, <sup>7</sup> H. Simgen, <sup>11</sup> C. Therreau, <sup>14</sup> D. Thers, <sup>14</sup> F. Toschi, <sup>13</sup> G. Trinchero, <sup>17</sup> C. Tunnell, <sup>24</sup> N. Upole, <sup>18</sup> M. Vargas, <sup>6</sup> O. Wack, <sup>11</sup> H. Wang, <sup>25</sup>

## (XENON Collaboration)

```
<sup>1</sup>Physics Department, Columbia University, New York, New York 10027, USA
               <sup>2</sup>Oskar Klein Centre, Department of Physics, Stockholm University,
                             AlbaNova, Stockholm SE-10691, Sweden
   ^3Nikhef and the University of Amsterdam, Science Park, 1098\mathrm{XG} Amsterdam, Netherlands
       <sup>4</sup>Department of Physics and Astronomy, University of Bologna and INFN-Bologna,
                                       40126 Bologna, Italy
    <sup>5</sup>Institut für Physik & Exzellenzcluster PRISMA, Johannes Gutenberg-Universität Mainz,
                                      55099 Mainz, Germany
 <sup>6</sup>Institut für Kernphysik, Westfälische Wilhelms-Universität Münster, 48149 Münster, Germany
     LIBPhys, Department of Physics, University of Coimbra, 3004-516 Coimbra, Portugal
          <sup>8</sup>New York University Abu Dhabi, 129188 Abu Dhabi, United Arab Emirates
                 <sup>9</sup>Physik-Institut, University of Zurich, 8057 Zurich, Switzerland
  <sup>10</sup>Department of Physics, Applied Physics and Astronomy, Rensselaer Polytechnic Institute,
                                   Troy, New York 12180, USA
                <sup>11</sup>Max-Planck-Institut für Kernphysik, 69117 Heidelberg, Germany
       <sup>12</sup>Department of Particle Physics and Astrophysics, Weizmann Institute of Science,
                                     Rehovot 7610001, Israel
            <sup>13</sup>Physikalisches Institut, Universität Freiburg, 79104 Freiburg, Germany
   <sup>14</sup>SUBATECH, IMT Atlantique, CNRS/IN2P3, Université de Nantes, Nantes 44307, France
      <sup>5</sup>Department of Physics, University of California, San Diego, California 92093, USA
         <sup>16</sup>INFN-Laboratori Nazionali del Gran Sasso and Gran Sasso Science Institute,
                                       67100 L'Aquila, Italy
           <sup>17</sup>INFN-Torino and Osservatorio Astrofisico di Torino, 10125 Torino, Italy
  <sup>18</sup>Department of Physics & Kavli Institute for Cosmological Physics, University of Chicago,
                                   Chicago, Illinois 60637, USA
       <sup>19</sup>Department of Physics "Ettore Pancini", University of Napoli and INFN-Napoli,
                                        80126 Napoli, Italy
<sup>20</sup>Kobavashi-Maskawa Institute for the Origin of Particles and the Universe, Nagoya University,
                     Furo-cho, Chikusa-ku, Nagoya, Aichi 464-8602, Japan
                   <sup>21</sup>Department of Physics and Astronomy, Purdue University,
                               West Lafayette, Indiana 47907, USA
             <sup>22</sup>LPNHE, Université Pierre et Marie Curie, Université Paris Diderot,
                                CNRS/IN2P3, Paris 75252, France
  <sup>23</sup>LAL, Université Paris-Sud, CNRS/IN2P3, Université Paris-Saclay, F-91405 Orsay, France
```

<sup>24</sup>Department of Physics and Astronomy, Rice University, Houston, Texas 77005, USA <sup>25</sup>Physics & Astronomy Department, University of California, Los Angeles, California 90095, USA



(Received 12 June 2019; published 25 September 2019)

The XENON1T experiment at the Laboratori Nazionali del Gran Sasso is the most sensitive direct detection experiment for dark matter in the form of weakly interacting particles (WIMPs) with masses above  $6 \text{ GeV}/c^2$  scattering off nuclei. The detector employs a dual-phase time projection chamber with 2.0 metric tons of liquid xenon in the target. A one metric ton  $\times$  year exposure of science data was collected between October 2016 and February 2018. This article reports on the performance of the detector during this period and describes details of the data analysis that led to the most stringent exclusion limits on various WIMP-nucleon interaction models to date. In particular, signal reconstruction, event selection, and calibration of the detector response to nuclear and electronic recoils in XENON1T are discussed.

DOI: 10.1103/PhysRevD.100.052014

### I. INTRODUCTION

The existence of a nonluminous, massive matter component beyond the standard model, called dark matter, is evidenced by numerous astrophysical observations [1]. Among the best-motivated dark matter candidates are weakly interacting massive particles (WIMPs) [2,3]. Ultrasensitive Earth-based detectors provide one possible approach to the direct detection of WIMPs as the particles are expected to scatter off the detector's target nuclei [4,5]. This induces nuclear recoils with mean energies in the order of a few keV.

Experiments that employ the liquid xenon (LXe) time projection chamber (TPC) technology are leading the search for elastic WIMP-nucleon interactions for masses from a few  $\text{GeV}/c^2$  up to the  $\text{TeV}/c^2$  scale [6–8]. The XENON1T experiment [9] has placed the most stringent upper limit on the spin-independent WIMP-nucleon cross section for masses above 6  $\text{GeV}/c^2$  with a minimum of  $4.1 \times 10^{-47} \, \text{cm}^2$  at 30  $\text{GeV}/c^2$  and 90% confidence level [6].

Together with Ref. [10], this document reports on the analysis methods employed for the spin-independent dark matter search with XENON1T and subsequent results [11,12]. While the present article describes the techniques of signal reconstruction, event selection, and detector calibration, details on the detector response model, the WIMP signal and background models, and the statistical inference are presented in Ref. [10].

The XENON1T detector was hosted by the Laboratori Nazionali del Gran Sasso and was operated with a total of approximately 3200 kg of ultrapure LXe, with (2004  $\pm$  5) kg contained in the TPC as an active target and the remainder used for shielding. Additional shielding from ambient radioactivity was provided by a 10 m tall and 9.6 m diameter water

tank that served as active Cherenkov muon veto [13] and passive shielding. The TPC was cylindrically shaped with a diameter of 96 cm and height of 97 cm. The top and bottom surfaces were instrumented by arrays of 248 Hamamatsu R11410-21 low-background photomultiplier tubes (PMTs) of 3 in. diameter in total [14,15].

Particles scatter off xenon atoms inducing either nuclear recoils (NRs) or electronic recoils (ERs). The recoil energy is measured by detecting signals from excitation and ionization of xenon atoms, in which the relative contribution of these two channels depends on the recoil type. Excited xenon atoms emit 178 nm scintillation light [16], which is observed by the PMTs and is referred to as the S1 signal. The ionization electrons are extracted from the interaction site by an electric field and are drifted towards the liquid-gas interface at the top of the TPC where they are extracted into the gas phase by another, stronger electric field and create the proportional scintillation S2 signal [17]. S1 and S2 signals are anticorrelated due to the recombination of electrons with ions creating excited xenon atoms. The two signals are temporally separated by the drift time of the electrons, from which the z coordinate of the interaction is reconstructed. The x and y coordinates are inferred from the light pattern of the S2 signal on the top PMT array. The S2/S1 ratio is used to discriminate between ER background ( $\gamma$  and  $\beta$  radiation) and signal-like NR events (WIMPs and neutrons).

XENON1T was operated stably for more than one year from October 2016 to February 2018 (Sec. II). The raw data acquired during this period were converted into physical quantities such as peak amplitude, area, width, etc., by means of a data processor, which is described in Sec. III, together with an event simulation framework used to

<sup>\*</sup>Also at Institute for Subatomic Physics, Utrecht University, Utrecht, Netherlands.

Also at Coimbra Polytechnic - ISEC, Coimbra, Portugal.

<sup>&</sup>lt;sup>†</sup>constanze.hasterok@mpi-hd.mpg.de

ywei@physics.ucsd.edu

xenon@lngs.infn.it

evaluate the processor's performance. The processor also reconstructs the interaction position of each event (Sec. IV) and applies corrections to the measured signals to account for spatial dependencies (Sec. V). The search for WIMP dark matter is based on the selection of a clean sample of single-scatter events (Sec. VI) inside a central fiducial volume which features a reduced background level (Sec. VII). Finally, we present the detector response to NR and ER events in Sec. VIII.

## II. DETECTOR OPERATION AND STABILITY

## A. Science runs

XENON1T performed its first science run (SR0) between October 2016 and January 18, 2017, when a magnitude 5.7 earthquake temporarily interrupted the detector's operation. In SRO, the drift field yielded 120 V/cm with a rms of 8 V/cm averaged over a 1.3t fiducial volume (FV) (see Sec. VII). The second science run (SR1) was launched February 2, 2017. SR1 featured a lower drift field of 81 V/cm with a rms of 6 V/cm. The field was reduced as a consequence of high-voltage instabilities occurring after the earthquake. Compared to the improvement of the electron lifetime in SR1 (Sec. VA), this field reduction has a negligible impact on the analysis results in view of energy resolution and signal acceptance. The drift field is taken into account in the signal and background models [10], and the electric field values are determined from simulations, using finite element (COMSOL Multiphysics [18]) and boundary element methods (KEMField [19]). SR1 continued until February 24, 2018, marking over one year of stable data taking, as shown in Fig. 1. The blue line presents the accumulated dark matter live time vs calendar time, corrected for the data quality conditions described in Sec. VI A which reduce the live time by 13.6% and 6.9% in SR0 and SR1, respectively (see Table I).

In addition to science data acquisition, various calibration campaigns were performed as shown in Fig. 1 by the vertical colored bands. The <sup>220</sup>Rn decay chain includes the <sup>212</sup>Pb  $\beta$  decay, which is employed to calibrate the detector response to low-energy ER events for background modeling and to derive event selection criteria [20]. The metastable isotope <sup>83m</sup>Kr decays into its ground state by emitting 32.1 and 9.4 keV conversion electrons with half-lives of 1.83 h and 157 ns [21], respectively. Those decays are used to monitor spatial and time dependencies of detector signals (Sec. V) and reconstruct signal positions (Sec. IV B). The <sup>220</sup>Rn and <sup>83m</sup>Kr sources are injected into XENON1T via the gas purification loop. Shortly after injection, the isotopes are distributed homogeneously throughout the TPC [22]. To avoid potential impact on the position and signal correction from the nonuniformity of <sup>83m</sup>Kr events at the beginning of injection, the first hour data were not used for correction map generation. The acquisition of dark matter data was resumed after the calibration campaigns when the trigger rate had fallen to background level. In these science data, we also observed a trace amount of 83mKr events, which presumably was caused by a malfunction of the source valve. These events are not in the energy region of interest for standard dark matter searches but can be used to monitor the detector response throughout SR1.

A deuterium-deuterium plasma fusion neutron generator [23] and a vessel containing a <sup>241</sup>AmBe [9] source were immersed into the water tank next to the cryostat to calibrate the detector response to NR events for signal modeling.

Additionally, monoenergetic  $\gamma$  lines from radio impurities in the detector materials ( $^{60}$ Co and  $^{40}$ K) and xenon isotopes excited after neutron calibrations ( $^{129}$ mXe and

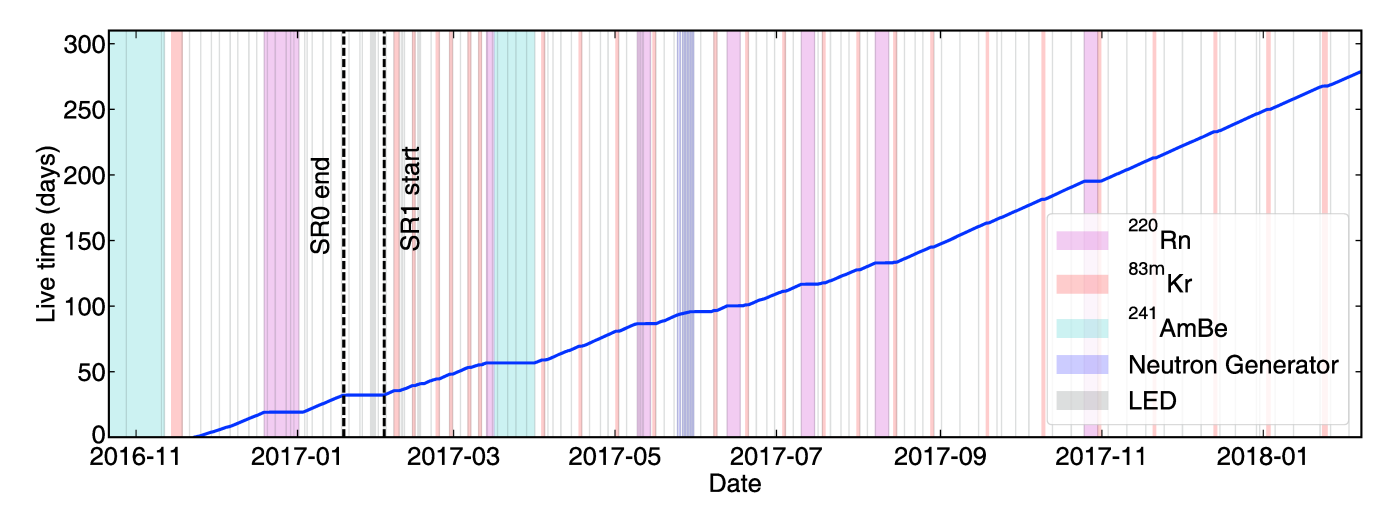


FIG. 1. Accumulated data live time acquired with the XENON1T detector in dark matter search mode and corrected for data quality conditions (Sec. VI A). The black dashed vertical lines mark the end of SR0 and the start of SR1. The various colored bands represent periods of detector calibration with <sup>220</sup>Rn (magenta), <sup>83m</sup>Kr (red), <sup>241</sup>AmBe (cyan), and neutron generator (blue) sources and with blue LED light (gray).

 $1.938 \pm 0.001$ 

2

1

 $28.2 \pm 0.1$ 

TABLE I. Comparison of data live time attributes and detector operation parameters among the two science runs of XENON1T. The science data live time reduction refers to the fraction of data removed due to data quality criteria (Sec. VI A). The mean and  $1\sigma$  values of the detector operation parameters correspond to their temporal distribution, except for the electric fields where the mean and  $1\sigma$  refer to the spatial homogeneity. Note that PE is the abbreviation of photoelectron.

*		
Data live time attributes	SR0	SR1
Science data live time (days)	32.1	246.7
Science data live time reduction due to data quality (%)	13.6	6.9
Calibration live time (days)	39.2	83.6
Detector operation parameters	SR0	SR1
Drift field: FV-averaged (mean $\pm 1\sigma$ ) (V/cm)	$120\pm 8$	81 ± 6
Average electron lifetime (µs)	290	641
Extraction field: FV-averaged (mean $\pm 1\sigma$ ) (kV/cm)	$8.1 \pm 0.1$	$8.1 \pm 0.1$
Number [fraction (%)] of excluded PMTs	35 (14.1)	36 (14.5)
Liquid xenon temperature (mean $\pm 1\sigma$ ) (°C)	$-96.07 \pm 0.04$	$-96.02 \pm 0.02$

 $1.934 \pm 0.001$ 

2

1

 $27.2 \pm 0.9$ 

<sup>131m</sup>Xe) as well as the combined 41.5 keV conversion electron signal from <sup>83m</sup>Kr were used to monitor the detector stability and calibrate the energy scale over 3 orders of magnitude [9].

Xenon gas pressure (mean  $\pm 1\sigma$ ) (bar)

Charge yield: max. deviation from mean (%) Light yield: max. deviation from mean (%)

Single electron gain (mean  $\pm 1\sigma$ ) (PE/SE)

### **B.** Detector stability

During both science runs, the detector was operated under stable thermodynamic conditions that guarantee constant signal sizes.

In SR0 (SR1), the  $1\sigma$  fluctuations of the xenon gas pressure were within 0.05% (0.05%). The pressure was uniformly distributed inside the detector, which also reflected on the stability of the single electron (SE) gain, i.e., the size of S2 signals from SE extracted from the liquid into the gas phase. The SE gain is determined by the gas pressure, the LXe level, and the electric extraction field. SE signals are identified similarly to the procedure described in Ref. [24], and the extracted SE gain has an average of 27.2 photoelectrons (PE)/SE (28.2 PE/SE) and a  $1\sigma$  time variation of 3.2% (0.5%) in SR0 (SR1) and a SE  $1\sigma$  width of 7.3 PE/SE (7.4 PE/SE) with a time stability of 11% (5%). The slightly larger variation in SR0 is caused by small fluctuations of the LXe level. The fluctuation of the LXe temperature was within 0.04% (0.02%) for SR0 (SR1). The temperature difference between the top and bottom of the TPC was within 0.25°C. The potential impact of the temperature variation on signal yields was taken into account by the signal corrections in Sec. V. Table I lists the most important detector operation parameters and their  $1\sigma$ spread around the temporal mean value.

The PMT gains were measured weekly with a pulsed blue light-emitting diode (LED) configured to stimulate the emission of a low number of PEs from the photocathode, and the gains are extracted using the model-independent approach described in Ref. [25]. Figure 2 shows the gain evolution of three stable PMTs (104, 108, and 133) that are representative for the majority of PMTs in the XENON1T TPC. In SR0 (SR1), 35 (36) PMTs were excluded from analysis [26], with 15 (15) in the top and 20 (21) in the bottom array. Nearly all of these PMTs suffered from vacuum leaks causing decreased performance such as light emission and afterpulses, requiring the bias voltage of the PMT to be lowered, eventually to zero. The criterion for exclusion from analysis is a single photoelectron (SPE) acceptance smaller than 50% [9]. Although vacuum leaks led to the decrease of PMT gains, 19 PMTs with small leaks were operated successfully throughout the science runs, and their gains were monitored and corrected. Two examples, PMTs 61 and 142, are shown in Fig. 2. The gain evolution is modeled empirically by Fermi-Dirac functions that take into account the time when the PMT high-voltage was lowered. The standard deviation of the measured gain with respect to the model is within a few percent for both stable and decreasing PMT gains and is dominated by statistical uncertainties. Compared to the approximately 27% resolution of the PMT response to SPEs [14], the systematic uncertainty of the gain has negligible impact on the energy resolution.

The temporal stability of the S1 and S2 signals is further confirmed by monitoring the light and charge yield (LY and CY, respectively) evolution over time. Using data from monoenergetic sources between 9.4 keV (83mKr) and 5.6 MeV (222Rn), the measured S1 and S2 signals per incident energy are evaluated following the same procedure as in Ref. [9]. The values are stable throughout both science runs with maximum deviations from the mean of 1% and 2%, respectively.

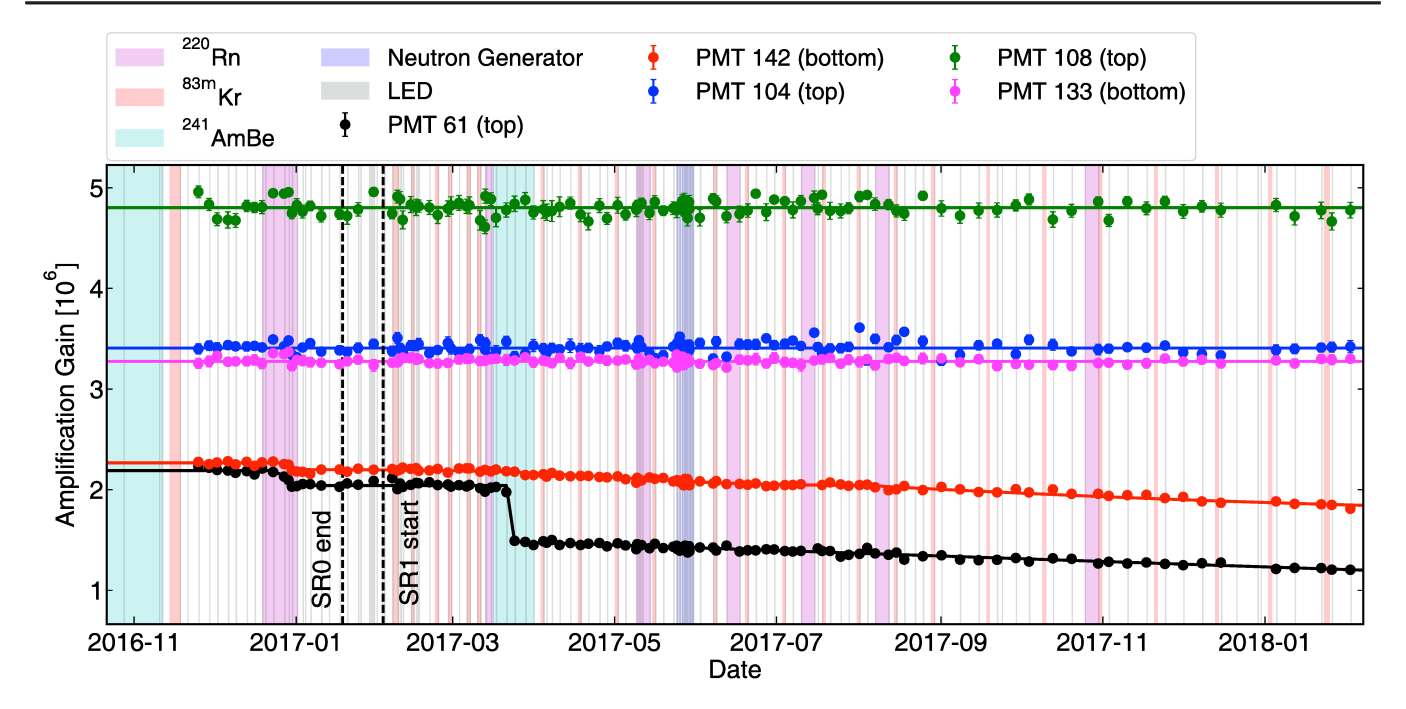


FIG. 2. PMT gains measured by LED calibrations as a function of time for three representative stable PMTs (green, blue, and magenta) and two examples in which the gain decreased due to small vacuum leaks (red and black).

## III. SIGNAL RECONSTRUCTION AND SIMULATION

PMT signals exceeding a channel-specific threshold above the baseline, accepting on average 93% of SPE signals, are digitized at a rate of 108 samples/sec by the data acquisition (DAQ) system [27]. These signals are referred to as *pulses*. An online event builder groups pulses into events using a simplified algorithm to trigger on S1 and S2 candidates and stores a 1 ms window around each trigger. During offline processing by the custom developed data processor PAX [28], pulses are further segmented into smaller intervals, denoted as hits, by separating individual signals, which may have been grouped into the same pulse waveform. Hits from different PMT channels are grouped into clusters in time, referred to as peaks, and corresponding to individual ionization or scintillation signals. Properties of each peak, such as area, width, and height, are computed by the processor. A peak is classified as S1 (S2) if its waveform rises sufficiently fast (slow) and has at least 3 (4) contributing PMTs. For S1s, only hits with maxima within a 100 ns window centered on the maximum of the sum waveform for all channels are counted for the latter requirement. Finally, each event is searched for a valid S1-S2 pairing, starting with the largest peaks of each type. These pairings are called *interactions*. A further reduction of the processor output is performed by the software package HAX [29]. Signal corrections (Sec. V) as well as other higher-level algorithms are included at this level.

The performance of the data processor is studied using emulated PMT signals from a waveform simulator.

The simulation employs data-driven models of XENON1T detector-specific properties like the scintillation light pulse shape, the spatial dependence of the light collection efficiency, the diffusion of electrons during drift, the time profile of SE, PMT afterpulses, the SEs generated by photoionization of impurities, and the electronic noise. The simulated data are validated by comparison to <sup>83m</sup>Kr and neutron calibration data and provide the means to optimize the reconstruction algorithms in the data processor and quantify their performance.

The S1 signal reconstruction efficiency is determined from simulated waveforms and is shown in Fig. 3. The efficiency is a function of the number of PMT hits, which at low energies is equivalent to the number of detected photons. The conversion into the S1 peak area (shown in the top axis of Fig. 3) assumes a double electron emission probability at the PMT's photocathode of 21.9% [10]. The efficiency's uncertainty is estimated from the simulation by varying the data-driven model parameters S1 width, PMT afterpulse rates, and rate of photoionization at the gate within their uncertainties. The results are cross-checked with a datadriven method, of which subsets of hits from a large S1 are selected to build an artificial low-energy S1, and the efficiency is calculated based on these low-energy artificial S1s. The result from the data-driven method using <sup>220</sup>Rn calibration is in agreement with simulations as shown in Fig. 3. Compared to SR1, the S1 efficiency for SR0 is slightly smaller at the threshold due to a higher PMT noise level in the first third of SR0 dark matter data acquisition that could be reduced by installing low-pass filter boxes at the PMT high-voltage modules [27].

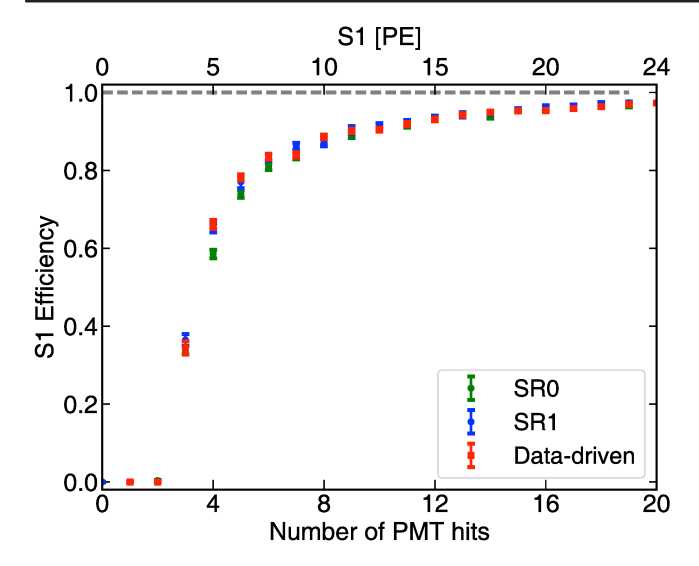


FIG. 3. S1 signal reconstruction efficiency estimated from waveform simulations, as a function of number of PMT hits. Hits are converted into S1 signal size (top axis) using a double PE emission probability at the photocathode of 21.9% [10]. The data-driven efficiency from <sup>220</sup>Rn calibration is overlaid for comparison.

The S2 trigger efficiency of the offline event builder is determined by applying the trigger algorithm to simulated S2 waveforms that were generated homogeneously throughout the TPC. The analysis threshold for S2 signal sizes is fixed to 200 PE, where the trigger efficiency yields  $(99.8^{+0.2}_{-0.6})\%$  and  $(99.4^{+0.4}_{-0.7})\%$  in SR0 and SR1, respectively, and the S2 size is defined using the sum of the signals from the top and bottom PMT arrays. Recently, a data-driven method became available and resulted in about 4% smaller efficiencies at the S2 signal threshold [27]. However, this is expected to have no noticeable impact on the dark matter search since the S1 signal reconstruction efficiency is the dominating parameter determining the detection threshold.

The bias B in reconstructing peak area is estimated by simulating homogeneously distributed S1 and S2 peaks. The expected number  $A_{\text{true}}$  of detected PEs of a given peak is compared with the number  $A_{\text{rec}}$  of reconstructed PEs:

$$B = (A_{\text{rec}} - A_{\text{true}})/A_{\text{true}}.$$
 (1)

The reconstruction bias is predominantly caused by signals from photoionization, particularly coming from the gate electrode, and afterpulse signals in the PMTs. These signals can be merged to or cut off from the primary peak. Figure 4 shows the mean and  $1\sigma$  width of the Gaussian-shaped distribution of B as functions of S1 and S2 signal sizes. The uncertainty bands are estimated following the same procedure as for the S1 reconstruction efficiency. The mean bias and its width are very similar for the two science runs in the case of S1 signals. However, the two parameters are slightly higher for S2 signals measured in SR1 compared to those in SR0. This difference is most likely caused by a higher PMT afterpulse rate in SR1 as a result of increasing PMT vacuum leaks as explained in Sec. II B.

The S1 reconstruction efficiency and S1 and S2 signal reconstruction biases are input parameters for the signal and background response models [10].

## IV. POSITION RECONSTRUCTION AND RELATED CORRECTIONS

Three-dimensional position reconstruction is one of the main advantages of dual-phase TPCs. Most radiogenic background events are located near the boundaries of the TPC and are rejected by selecting a radio-pure inner fiducial volume (Sec. VII). In addition, accurate position reconstruction is required for the development of background models [10] and for position-dependent signal corrections (Sec. V).

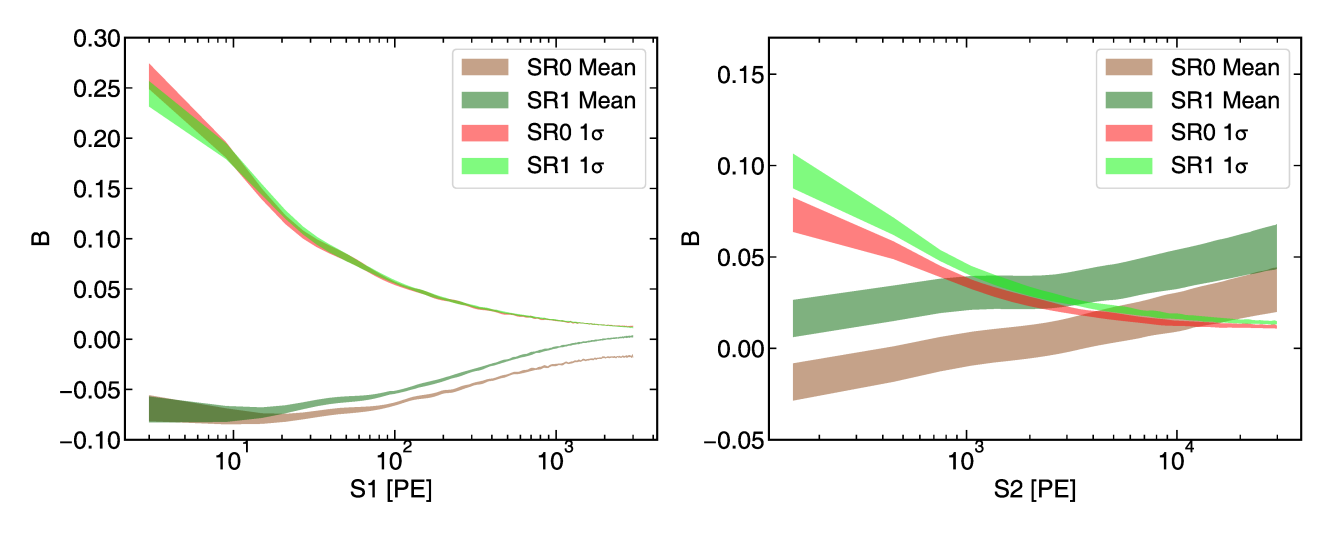


FIG. 4. S1 (left) and S2 (right) signal size reconstruction bias B and its  $1\sigma$  width as estimated from simulations. The bands are derived by varying the data-driven model parameters within their uncertainties and hence represent the credible region of the shown values.

### A. Position reconstruction methods

The vertical coordinate  $z_{\rm obs}$  (the subscript obs indicating the position before correction as described in Sec. IV B) of an interaction is determined by the electron drift velocity and the time difference between the prompt S1 and the delayed S2 signal. The origin of the coordinate is at the gate electrode, and the TPC height extends down to -97 cm. Because of the diffusion of the electron cloud during the drift, multiple scatter events with close proximity in z are more difficult to separate at the bottom of the TPC than at the top. By identifying multiple scatter events in NR calibration data, the distance in z for the two interactions is determined. The distribution features a roll-off for small z distances varying with the interaction depth. The minimal value for which two scatters are separable with an acceptance of 50% is found to increase from 2 mm at the gate to 7 mm at the cathode for S2 signals in the region of interest for dark matter searches (S2 < 25000 PE).

The horizontal position ( $[x_{obs}, y_{obs}]$  or  $[R_{obs} = \sqrt{x_{obs}^2 + y_{obs}^2}, \phi_{obs}]$ ) is obtained from the hit pattern of the S2 signal on the top PMT array. The origin in the x-y plane is set to the center of the TPC. Several position reconstruction algorithms are employed in LXe detectors, such as artificial neural networks (NN) [30], top pattern fit (TPF) [31], support vector machine [32], and statistical light response functions [33]. In XENON1T, a NN is trained using the open-source Fast Artificial Neural Network Library (FANN) [34]. In addition, a TPF algorithm serves as a cross-check for identifying events with poorly reconstructed positions (Sec. VI).

To calibrate the algorithms, data from an optical Monte Carlo (MC) simulation is used. Training data are generated by propagating photons over the full detector geometry [35], which is implemented using the GEANT4 toolkit [36]. Optical parameters such as the refractive index, PTFE (polytetrafluoroethylene, Teflon) reflectivity, xenon absorption length, and Rayleigh scattering length are tuned by matching the simulated light collection to <sup>83m</sup>Kr calibration data.

## **B.** Field distortion correction

Reconstructed spatial distributions exhibit a radial inward bias with increasing depth due to the distortion of the electric drift field and repulsive effects of accumulated negative charges on the lateral PTFE reflector panels that confine the TPC. Figure 5 illustrates this effect integrated over the  $z_{\rm obs}$  coordinate. The  $x_{\rm obs}$ - $y_{\rm obs}$  distribution for  $^{83\rm m}$ Kr data exhibits a regular geometric distortion from the physical TPC boundary that can be related to the PTFE panel configuration. The distortion is largest at the locations of the 24 panels (black segments) that are not in contact with the ring-shaped copper electrodes surrounding the TPC for drift field shaping [9]. The distortion is smallest at the smaller panels (magenta segments), which are in contact with the electrodes. Figure 6 shows the position of

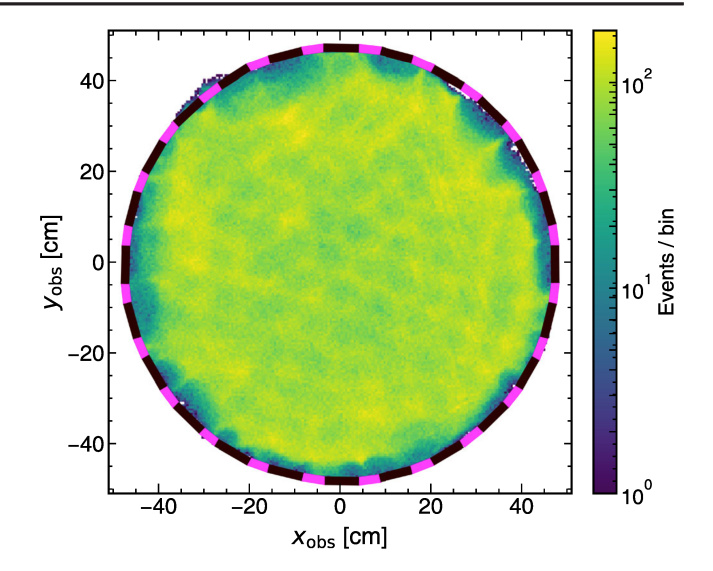


FIG. 5.  $x_{\rm obs}$ - $y_{\rm obs}$  distribution of  $^{83\rm m}$ Kr events as reconstructed by the FANN algorithm integrated over  $z_{\rm obs}$ . The distortions at high radii coincide with the 24 PTFE reflector panels (black segments) that are not in contact with the ring-shaped electrodes surrounding the TPC for drift field shaping. Magenta segments indicate the panels that are in contact with the electrodes.

the TPC edge in bins of  $z_{\rm obs}$  by open markers for several periods throughout the science run, indicating an increasing accumulation of charges during detector operation. The data are derived from the radial distribution of signals from  $^{222}$ Rn progeny on the PTFE surface. Those signals are referred to as surface events [10]. The error bars in the  $R_{\rm obs}$  direction indicate the event distribution's radial width, while the error bars in  $z_{\rm obs}$  mark the bin width.

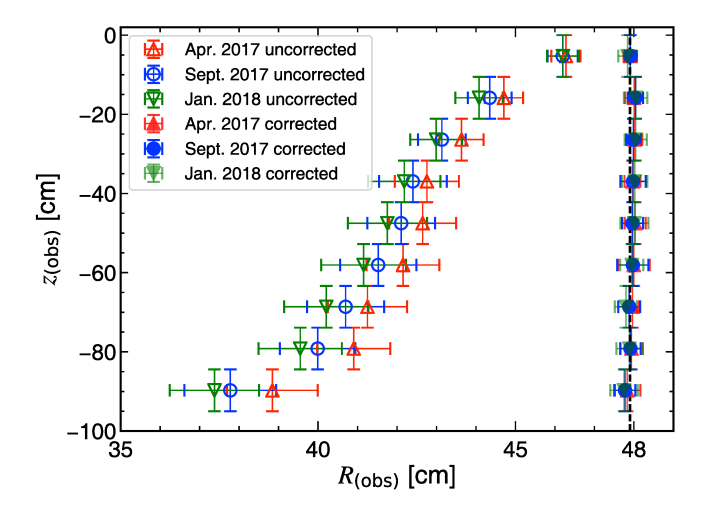


FIG. 6. Maximum TPC radius reconstructed from signals of surface events in three time intervals and in bins of z. Open (filled) markers show radii before (after) position correction. Horizontal error bars indicate the radial width of the event distribution. Vertical error bars mark the z bin width. The black dashed vertical line indicates the geometrical TPC radius.

The first WIMP dark matter results of XENON1T [26] using data recorded in SR0 featured a two-dimensional correction of reconstructed positions ( $R_{obs}$ ,  $z_{obs}$ ) based on a matching of the uniform spatial distribution of <sup>83m</sup>Kr events to the distribution predicted by electric field simulations performed with the COMSOL Multiphysics package [18]. This correction is sufficient for a fiducial mass of up to 1t since the contribution from surface events is negligible in the corresponding volume. During the analysis of SR1 data, an improved understanding of the field distortion and its time evolution was obtained, which led to a 83mKr datadriven correction in three dimensions  $(R_{\rm obs}, z_{\rm obs}, \phi_{\rm obs})$  for four time intervals throughout SR0 and SR1. To derive the correction, the detector is segmented into 180 bins in  $\phi_{\rm obs}$  and 40 bins in  $z_{\rm obs}$ . The event positions in each bin are corrected such that they are evenly spaced in the square of the corrected radial position  $R^2$ . Corrected depths z are subsequently obtained by the geometric relation z =

 $-\sqrt{z_{\rm obs}^2-(R-R_{\rm obs})^2}$ . The position correction is validated with spatially homogeneous signals from decays of  $^{131{\rm m}}$ Xe activated by neutron calibrations as well as nonuniform sources, such as neutron calibration signals, which are compared to MC simulations. A Kolmogorov-Smirnov test [37] yields a goodness of fit p value of 0.55 when comparing  $^{131{\rm m}}$ Xe event positions to a uniform distribution.

The impact of the correction is illustrated in Fig. 6. Filled markers indicate the corrected radial position of the TPC edge in bins of z. After correction, the position of surface events coincides with the maximal radial position.

## C. Radial position resolution

The position resolution in the radial dimension is dependent on the S2 signal size as well as on the radial event position due to nonfunctional PMTs and light reflection at the TPC boundary.

The two consecutive <sup>83m</sup>Kr decays provide a sample to show the radial position resolution as a function of R for fixed S2 signal sizes. Events in the upper approximately 5 cm of the TPC are selected, as only in that region the two S2 signals can be resolved. The spatial separation of the signals can be neglected with respect to the uncertainty from the reconstruction method. The average path length of the 9.4 keV conversion electrons in LXe is only approximately 10  $\mu$ m, and the small half-life of 157 ns does not allow for a reconstructable drift of the atoms by convection. The mean of the distribution of the absolute radial difference  $(\Delta R = |R_{32.1} - R_{9.4}|)$  between the 32.1 and 9.4 keV signals is shown in bins of  $R^2$  in Fig. 7. The vertical error bars display the distribution's standard deviation. Note that the position reconstruction uncertainties from both decays are convoluted in  $\Delta R$ . Hence, a direct comparison to the resolution of single events is not possible. While the precision in reconstructed radial positions is in the order

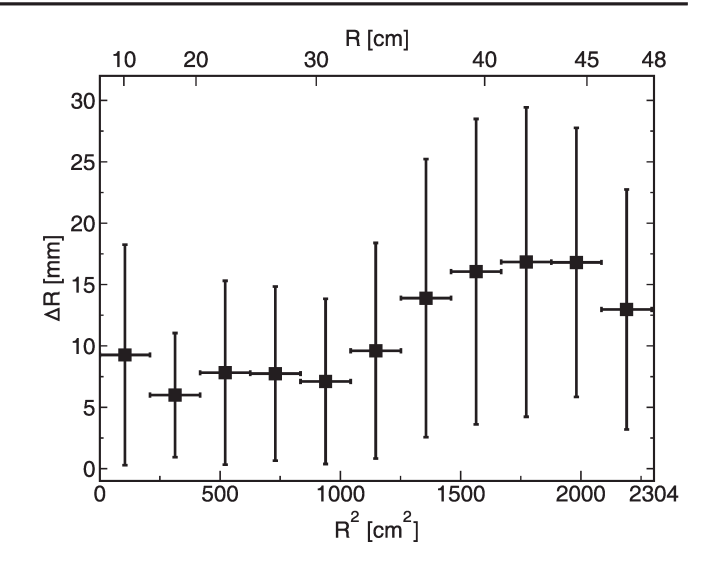


FIG. 7. Absolute radial difference ( $\Delta R$ ) reconstructed between 32.1 and 9.4 keV signals from <sup>83m</sup>Kr in bins of  $R^2$ . The corresponding R scale is shown on the upper horizontal axis. The vertical error bars represent the standard deviation of the  $\Delta R$  distribution, while horizontal error bars indicate the  $R^2$  bin width.

of approximately 1 cm for R < 35 cm, the performance declines by a factor of 1.5 toward larger radii. This is caused by nonfunctional PMTs and light reflection at the TPC boundary as mentioned above.

In addition to the radial dependence of the position resolution for fixed S2 signal sizes, we also investigated its dependence on S2 signal sizes for a fixed position. Surface events provide a sample at the maximum TPC radius and cover a large range of S2 signals down to less than 200 PE due to charge loss. Figure 8 shows the standard deviation  $\sigma_R$  of the radial distribution in bins of S2 signal size. The uncertainties are derived from the Gaussian fit, and

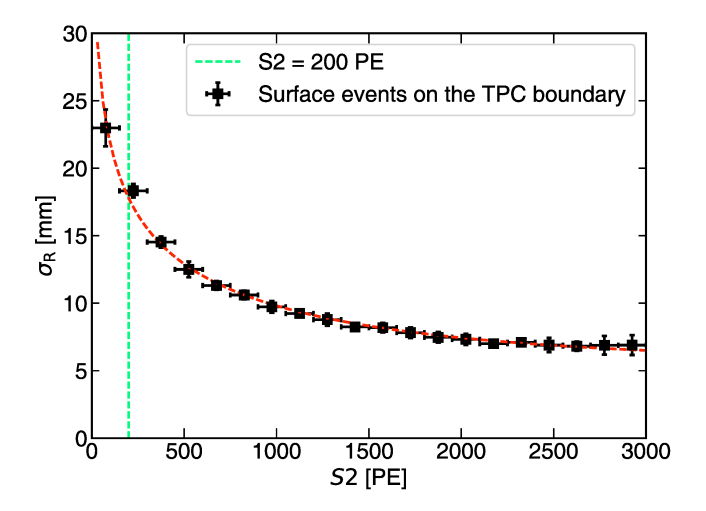


FIG. 8. Radial position resolution  $\sigma_R$  in bins of S2 signal size for surface events. Vertical uncertainties are derived from the Gaussian fit, while horizontal error bars mark the S2 bin width. The red dashed line indicates the best fit of an empirical function.

horizontal error bars mark the S2 bin width.  $\sigma_R$  yields 1.9 cm at the S2 analysis threshold of 200 PE and decreases to values less than 0.8 cm for large S2 signal sizes. The resolution is limited by the accuracy of the optical MC simulation used to train the FANN. Note that the resolution is poorest for surface events due to their location at high radii (Fig. 7) and is expected to improve for interactions in the center of the TPC.

The presented position resolution studies are considered in the background and signal models for final inference of the dark search data [10].

#### V. SIGNAL CORRECTIONS

The size of the recorded S1 and S2 signals depends on the event location in the detector due to various position-dependent effects, such as electron attachment to impurities in the LXe target, light collection efficiency, field inhomogeneities, variations of the thickness of the proportional scintillation region and nonfunctioning PMTs. In the following, the corrections applied to S1 and S2 signals in order to account for these effects are explained. The corrected signals are denoted as cS1 and cS2.

#### A. Electron lifetime correction

The loss of ionization electrons due to attachment to electronegative impurities (e.g.,  $O_2$ ) [38] in LXe is a function of the drift time and follows an exponential law with the electron lifetime  $\tau_e$  as a decay parameter. This effect is the most important correction for S2 signals and is highly dependent on the impurity concentration in the target. Since the xenon is continuously purified,  $\tau_e$  is a parameter changing over time and has to be continuously monitored [9].

The electron lifetime is evaluated in intervals of two to three weeks by measuring the 41.5 keV signal from the two consecutive 83mKr decays as a function of electron drift time. Additionally,  $\tau_e$  is estimated from monoenergetic  $\alpha$ decays of <sup>222</sup>Rn and <sup>218</sup>Po observed in background data that provide sufficient statistics on a daily basis. The  $\tau_e$  values from these two methods are shown in Fig. 9 and feature an offset of up to 10% of unknown origin that scales with the xenon purity. The best hypothesis of the discrepancy is related to the small inhomogeneity of the drift field. The ionization yield of  $\alpha$  decays has stronger field dependence than ERs and NRs; hence, the measured  $\tau_e$  are different. Because the energy from 83mKr decays is closer to the region of interest for dark matter searches compared to  $\alpha$ decays, furthermore, better energy resolution up to the MeV scale and better discrimination between ER and NR signals (Sec. VIII) can be achieved when applying  $\tau_e$  derived from <sup>83m</sup>Kr decays in the S2 signal correction, we decided to use the  $\tau_e$  from  $^{83\text{m}}\mathrm{Kr}$  decays for the final corrections.

The temporal fine structure of the electron lifetime evolution is modeled based on  $\alpha$  decays by fitting a model that estimates the evolution of impurity concentrations in the gaseous and LXe phase and takes into account various detector operation parameters like the detector's cooling power and the xenon gas flow in the purification system [39]. The model's best fit (uncertainty) is shown by the gray line (band) in Fig. 9. During the two science runs of XENON1T, several decreases of electron lifetime that coincide with releases of impurities due to changes in the above-mentioned parameters were observed.

The absolute scale of the electron lifetime model is derived by relating the  $1/\tau_e$  data points from the two methods by a linear function which is used to scale from the  $\alpha$  measurement to the  $^{83}$ mKr measurement. The final

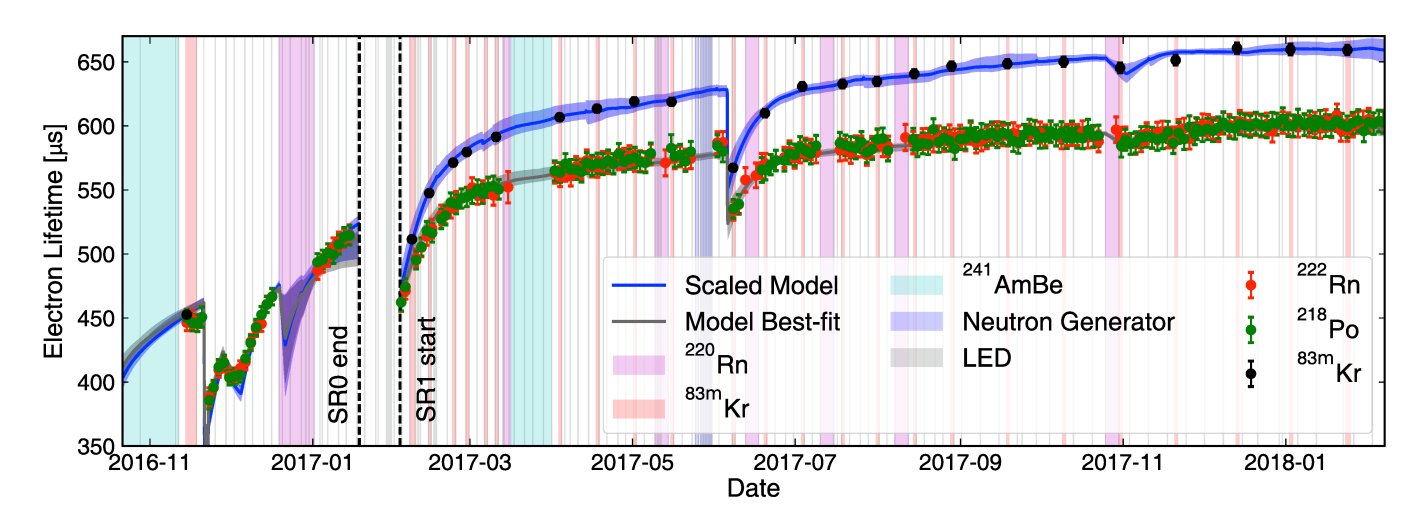


FIG. 9. Electron lifetime evolution during the two science runs measured from  $^{83\text{m}}$ Kr (black),  $^{222}$ Rn (red), and  $^{218}$ Po (green) decays. Decreases are caused by releases of impurities due to changes in detector operation parameters like the detector's cooling power and the gas flow in the purification system. The temporal fine structure is modeled based on the  $\alpha$  measurements (gray line), while the absolute scale of the electron lifetime is determined from the  $^{83\text{m}}$ Kr measurement.

electron lifetime model used for S2 signal correction is shown by the blue solid line together with its uncertainty band.

During SR1,  $\tau_e$  leveled off at about 650  $\mu$ s, corresponding to an oxygen equivalent impurity concentration of about 0.5 ppb limited by outgassing materials and the flow in the gas purification circuit.

## **B. S2 spatial correction**

The proportional scintillation signal S2 is produced between the liquid-gas interface and the anode electrode. The fraction of the total S2 signal measured by the top PMT array is  $(63\pm2)\%$ . The signal detected in the top array is highly localized, while the bottom PMT array provides a more uniform distribution that is more resilient to effects from nonfunctional PMTs or variable light collection efficiency. For this reason, only the corrected bottom array signal, cS2<sub>b</sub>, is used in the final inference of dark matter search data.

Positional variations in the S2 size arise due to distortion of the electric field at the liquid-gas interface induced by subsidence of the anode caused by its weight, impacting the electron extraction efficiency. These variations are corrected using the 41.5 keV charge signal of  $^{83\text{m}}$ Kr. The  $x_{\text{obs}}$ - $y_{\text{obs}}$  distribution of S2 signals is fit by a two-dimensional second-order polynomial. The best-fit value of the function's center for S2 signals observed by the bottom array is displaced from the origin by about 1.5 cm to negative  $x_{\text{obs}}$  and  $y_{\text{obs}}$  values. This displacement indicates a slight tilt of the TPC. The extraction efficiency is approximately 20%–30% lower at the edge of the detector compared to the center, while the average value yields 96% [9].

## C. Light collection efficiency

The LY is impacted by the light collection efficiency  $\epsilon_L$ , i.e., the number of photons that hit a PMT photocathode per photon emitted at the interaction site; the photon yield (PY), i.e., the number of generated photons per incident energy  $\epsilon$ ; the PMT quantum efficiency  $\epsilon_{\rm QE}$ , i.e., the probability that one photon hitting the photocathode induces one PE; and the collection efficiency  $\epsilon_{\rm CE}$  of photoelectrons within the PMT:

$$\frac{\mathrm{S1}(R,\phi,z,\varepsilon,F)}{\varepsilon} = \mathrm{LY}(R,\phi,z,\varepsilon,F)$$

$$= \varepsilon_L(R,\phi,z) \cdot \mathrm{PY}(\varepsilon,F(R,\phi,z,t)) \cdot \varepsilon_{\mathrm{QE}} \cdot \varepsilon_{\mathrm{CE}}.$$
(2)

 $\epsilon_L$  is affected by the number of photon reflections before reaching a PMT photocathode and is, therefore, spatially dependent. The PY depends on the energy and the drift field F, which both impact the electron-ion recombination [40]. The field features variations at the TPC edges, which

vary in time *t* due to charge accumulation on PTFE surfaces (see Sec. IV).

To correct for the spatial dependence of S1 signals, a three-dimensional correction map is derived from the 32.1 keV signals in  $^{83\text{m}}$ Kr calibration data. The mean of the S1 distribution is evaluated in discrete  $(R, \phi)$  regions and in slices of z and is normalized to its average  $\langle \text{S1} \rangle$  across the TPC in order to obtain the relative light collection efficiency  $L_c$  that removes the spatial dependencies:

$$\begin{split} \frac{LY(R,\phi,z,\varepsilon,F)}{L_c(R,\phi,z)} &= \langle LY(\varepsilon,F) \rangle \\ &= \langle \varepsilon_L \rangle \cdot \langle PY(\varepsilon,F(R,\phi,z,t)) \rangle \cdot \varepsilon_{\text{QE}} \cdot \varepsilon_{\text{CE}}. \end{split} \tag{3}$$

The number of bins of the correction map was optimized in each dimension by limiting the maximum variation to be about 2.5% between two adjacent bins. The correction not only averages out the spatial dependence of  $\epsilon_L$  but also accounts for the spatially dependent PY introduced by field inhomogeneities.

 $^{83\text{m}}$ Kr decay energies lie beyond the region of interest for WIMP searches, and lower-energetic events are less sensitive to changes in the field. Hence, a small bias of approximately 2% [40] is introduced when applying  $L_c$  to the WIMP search region, and  $L_c$  varies in time by up to 6% due to evolving field inhomogeneities (Sec. IV B). To remove this bias, the spatial distribution of the CY from the 41.5~keV  $^{83\text{m}}$ Kr signal is used to map out local and timely field variations and decouple those from both the  $L_c$  and electron lifetime corrections. Since the CY is correlated with the electron lifetime, this procedure is repeated iteratively until convergence is observed resulting in a time stability of  $L_c$  within 1.2%.

Figure 10 shows  $L_c$  measured as a function of z (left) and  $\phi$  (right) for bins in R. The largest variation is observed along z with a maximum  $L_c$  at the bottom center of the detector where the solid angle to the bottom PMT array is largest.

## VI. SELECTION CRITERIA AND THEIR ACCEPTANCES

This section describes the criteria applied to the dark matter search data for selecting single scatter events in the region confined by  $cS1 \in [3,70]$  PE and  $cS2_b \in [50,7940]$  PE corresponding to the energy region of interest, [1.4,10.6] keV<sub>ee</sub> ([4.9,40.9] keV<sub>nr</sub>) [6]. Note that the  $cS2_b$  was used in the analysis due to its uniform distribution as explained in Sec. V B. 50 PE of  $cS2_b$  correspond to 100% acceptance for the events with S2 over its 200 PE trigger threshold.

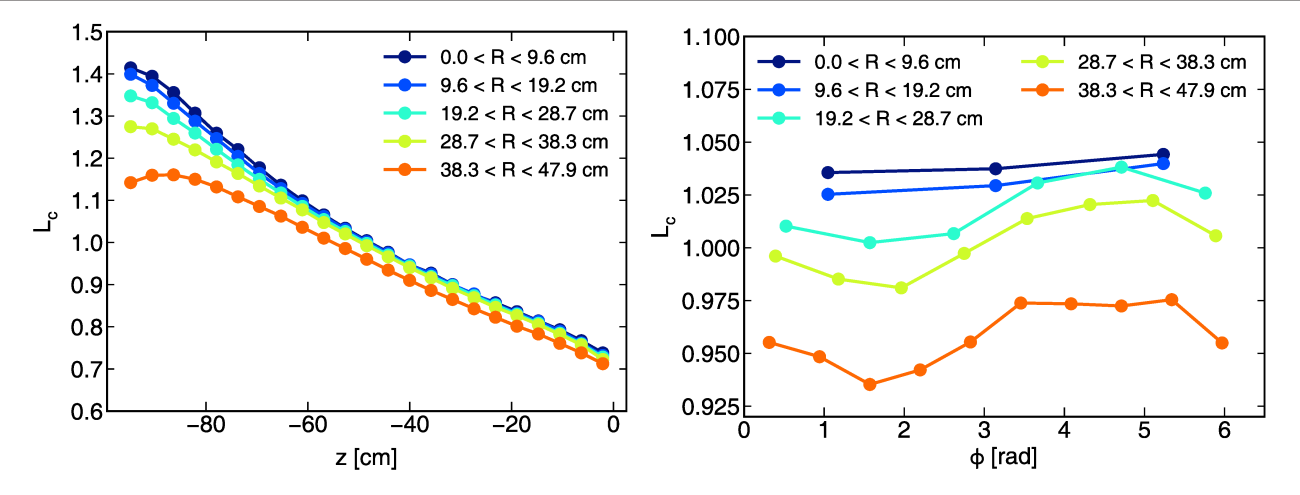


FIG. 10. Spatial dependence of the relative light collection efficiency  $L_c$  on z (left) and  $\phi$  (right) for different radial bins (color code). Data points are connected by straight lines to guide the eye.

## A. Data quality selection

Operational conditions during data acquisition are necessary for the rejection of certain time periods, regardless of the properties of the events contained within. The corrected live time and respective acceptance after the incremental application of four criteria are summarized in Table II.

The *DAQ veto* ensures that all channels in the DAQ system are able to record data. If this is not the case, a system-wide busy condition is issued. The start and stop times of the busy signal are saved in the data stream, ensuring that those time periods can be removed at the analysis level. The DAQ veto rejects about 6% (1%) of data in SR0 (SR1), with the increased dead time in SR0 caused by nonoptimized DAQ settings during the first XENON1T runs.

The active Cherenkov *Muon veto* triggers if at least eight PMTs in the water tank record signals larger than one PE within a 300 ns time window. Under these conditions, a muon tagging efficiency of 99.5% is achieved, while muoninduced shower events are identified with a probability of 43%. These efficiencies are determined from simulations, and the events are required to exhibit at least one produced neutron that has high enough energy (>10 MeV) to reach the TPC [13]. To remove signals from potential secondary interactions in the TPC, a muon veto trigger is searched in a

TABLE II. Summary of data live time and respective acceptance after incrementally applying data quality requirements in the shown order.

Data quality criterion	Live time (days)		Incremental acceptance (%)	
	SR0	SR1	SR0	SR1
Without cut	37.2	264.8	100	100
DAQ veto	34.2	261.6	92.1	98.8
Muon veto	33.5	259.1	90.0	97.8
Flash veto	33.5	258.8	89.9	97.7
S2 tails	32.1	246.7	85.8	93.0

window of [-2 ms, +3 ms] around each TPC event, which is rejected in case of success. The time range is conservatively determined from simulations [13] and data. In addition, all data are removed where the muon veto is inactive. In total, about 2% (1%) of live time after the DAQ veto is removed in SR0 (SR1) due to the muon veto criterion. The muon veto reduces the expected muoninduced neutron background rate by a factor of 2.5.

The XENON1T PMTs can emit bursts of light as previously observed in independent measurements [14]. In SR0 (SR1), a total of 8 (179) light flashes were observed, causing short periods of high pulse rates throughout the TPC from both the primary light and secondary interactions. These incidents are removed from the data by a *Flash veto* that scans the pulse rates for each PMT channel and identifies sudden, drastic increases. A conservative time window of 10 s before and 120 s after each flash is rejected. After the application of the DAQ and muon veto, the flash veto removes 0.04% and 0.12% of live time in SR0 and SR1, respectively. Flashes trigger in most cases the DAQ busy signal. Hence, the criterion is highly correlated with the reduction of live time due to the DAQ veto.

The S2 tails criterion addresses delayed S2 signals, e.g., from delayed electron extraction or photoionization on materials and impurities, which are generated especially after large S2s and do not correspond to physical interactions. Those can reduce the detector sensitivity to lowenergy interactions for several milliseconds. For each event, the discrimination variable  $S2_{pre}/\Delta t$  is defined as the ratio of the S2 size of a preceding event divided by the time difference to that event, where the preceding 100 events are scanned and the maximum of the parameter is stored. Figure 11 shows the distribution of primary S1 signal sizes vs  $S2_{pre}/\Delta t$  in single scatter events (Sec. VID) of background data, while a subset of noise rejection and reconstruction requirements (Sec. VIB) has been applied as

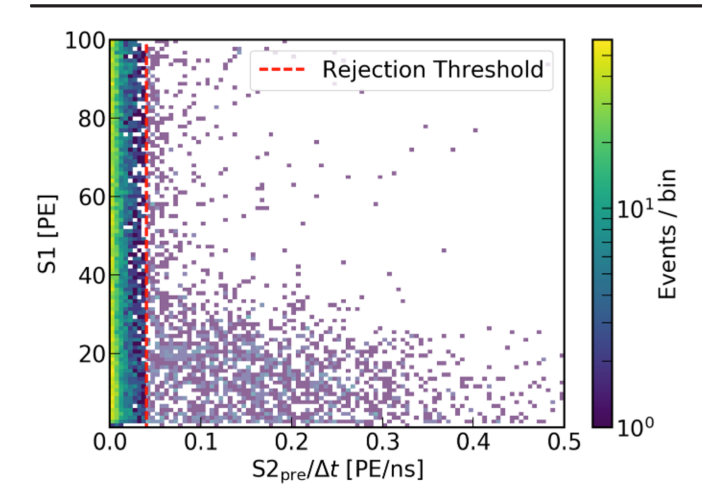


FIG. 11. Distribution of S1 signal sizes vs  $S2_{pre}/\Delta t$  as measured in  $^{220}$ Rn calibration data. The threshold in  $S2_{pre}/\Delta t$  above which events are rejected regardless of their own properties is indicated by the red line.

a preselection. Ionization signals from preceding events can be misidentified as an S1 or S2 of an interaction in subsequent events and therefore appear as a horizontal population in the figure. The  $S2_{pre}/\Delta t$  threshold above which an event is rejected is set to 0.04 PE/ns, which is chosen to remove the most intense region of increased activity while maintaining as much live time as possible. This removes 4% (5%) of live time in SR0 (SR1) in addition to the previously mentioned live time reductions.

#### B. Noise rejection and reconstruction requirements

A set of conditions is imposed to remove events that are either falsely reconstructed, members of known background populations, or generally of low quality:

- (i) If an event contains a large integral (>300 PE) of signals prior to the primary S2 excepting the primary S1, the event is deemed "noisy" and is removed.
- (ii) The contribution of one channel to an event's S1 is not allowed to exceed 5% of the S1 plus an offset of four PEs. This criterion prohibits that a single channel exhibiting a PMT malfunction dominates the signal. Typical causes for failing the condition are PMT afterpulses or light emission.
- (iii) S2s originating from single electron signals can be misclassified as S1s at the data-processor level. This can result in events in which two S2 signals, one misidentified and one lone signal, are randomly paired as an interaction. Lone S2 signals originate from delayed electron extraction and pileup and therefore do not feature a corresponding S1. Two machine-learning classification algorithms, a boosted decision tree and a random forest from the SCIKIT-LEARN PYTHON package [41], are employed to

reclassify S1s based on the most important peak properties of width, area, rise time, and signal fraction detected in the top PMT array. Training samples for good S1s are selected from high-quality background events in the ER band and from sampling hits from larger S1 signals, effectively creating smaller signals in the region of interest. Single electron S2 training samples are created by selecting S2 peaks that are isolated from other signals by at least  $10~\mu s$ . The threshold for removing an event, placed on the classifier's normalized voting, was optimized to achieve a reduction of S2 signals misclassified as S1 signals by a factor of 5.

- (iv) The almost constant fraction of light from S2 signals observed by the top PMT array is used to reject background caused by interactions in the gas phase above the anode electrode or from misreconstructed events. High-quality calibration events are used to model the distribution of true interactions in the liquid xenon depending on the S2 size. Events that exhibit an S2 light fraction in the top array that is smaller or larger than the 99% quantiles of the distribution are rejected.
- (v) Reliable position reconstruction is ensured by demanding the reconstructed  $x_{\rm obs}$ - $y_{\rm obs}$  coordinates to be consistent with the S2 hit pattern on the top PMT array. This criterion predominantly suppresses pileup of delayed electron signals, double scatters, or events that are misreconstructed at the wrong  $x_{\rm obs}$ - $y_{\rm obs}$  position, often due to nonfunctional PMT channels. The likelihood of the observed pattern given the position is computed using the same optical MC simulation as employed for the training of the position reconstruction algorithms.
- (vi) To further suppress anomalous  $x_{\rm obs}$ - $y_{\rm obs}$  reconstruction, events are removed if the difference in the reconstructed positions for the two reconstruction algorithms exceeds the upper 99% quantile of the position difference distribution defined in dependence of S2 size. This distribution is extracted from high-quality calibration data.

The acceptance of each cut described above is evaluated individually based on control samples either from calibration or background data. All data quality criteria together accept  $(95 \pm 4)\%$  of true signals that fall into the region of interest.

### C. S1-S2 signal correlation requirements

In each time window that is allocated to an event, the processor considers the largest S2 candidate and the S1 with the largest PMT coincidence level before the S2 as the primary interaction. This and the following criteria suppress pileup effects, double scatters, or accidentally pairing lone S1 and S2 signals that arise in charge- and light-insensitive detector regions: